Three-Order Tucker Decomposition and Reconstruction Detector for Unsupervised Hyperspectral Change Detection

Zengfu Hou, Wei Li, *Senior Member, IEEE*, Ran Tao, *Senior Member, IEEE*, and Qian Du, *Fellow, IEEE*

***Abstract*—Change detection from multitemporal hyperspectral images has attracted great attention. Most traditional methods using spectral information for change detection treat a hyperspectral image as a two-dimensional matrix and do not take into account inherently structure information of spectrum, which leads to limited detection accuracy. To better approximate both spectral and spatial information, a novel three-order Tucker decomposition and reconstruction detector is proposed for hyperspectral change detection. Initially, Tucker decomposition and reconstruction strategies are used to eliminate the influence of various factors in a multitemporal dataset. Specifically, a singular value accumulation strategy is used to determine principal components in factor matrices. Meanwhile, a spectral angle is used to analyze spectral change after tensor processing in different domains. Finally, a new detector is designed to further improve the detection accuracy. Experiments conducted on five real hyperspectral datasets demonstrate that the proposed detector achieves a better detection performance.**

***Index Terms*—Change detection, hyperspectral imagery (HSI), principal components (PCs), singular value accumulation, tensor decomposition.**

I. Introduction

MULTITEMPORAL remote sensing images can be used to continuously observe and discover changed information of imaged scenes. Change detection is widely used in various military (e.g., missile early-warning and battlefield dynamic monitoring) and civil (e.g., environmental monitoring, land change, urban expansion, disaster detection, and evaluation) applications [1], [2]. Multitemporal hyperspectral images can provide fine and sophisticated spectral diagnostic information, which creates potentials for accurate change detection and identification of change types [3].

Manuscript received May 12, 2021; revised May 30, 2021; accepted June 8, 2021. Date of publication June 10, 2021; date of current version June 30, 2021. This work was supported in part by the National Natural Science Foundation of China under Grant 61922013 and Grant U1833203 and in part by Beijing Natural Science Foundation under Grant JQ20021 and Grant L191004. *(Corresponding author: Wei Li.)*

Zengfu Hou, Wei Li, and Ran Tao are with the School of Information and Electronics, Beijing Institute of Technology, Beijing 100081, China, and also with the Beijing Key Laboratory of Fractional Signals and Systems, Beijing 100081, China (e-mail: zengf.hou@bit.edu.cn; leewei36@gmail.com; rantao@bit.edu.cn).

Qian Du is with the Department of Electrical and Computer Engineering, Mississippi State University, Starkville, MS 39762 USA (e-mail: du@ece.msstate.edu).

Digital Object Identifier 10.1109/JSTARS.2021.3088438

Unlike multitemporal color or multispectral images, hyperspectral remote sensing simultaneously explores two-dimensional (2-D) spatial and one-dimensional (1-D) spectral information of ground objects. Therefore, change detection technology based on multitemporal hyperspectral images is more complex. Meanwhile, affected by various factors (seasons, terrain, weather conditions, solar altitude angle, etc.), there may exist spectral variations in unchanged pixels and changed information may be submerged in noise and background, which further increase the difficulty of change detection. Although various hyperspectral change detection methods are proposed according to different applications, these methods are still scarce compared to change detection methods for the multispectral remote sensing image.

The early change detection algorithms are mainly algebra-based methods [4], which are based on the assumption that changes cause obvious difference of pixel gray levels, and pixel by pixel analysis is adopted. These methods include image difference, image ratio, image regression, absolute distance (AD) [5], Euclidian distance (ED) [5], etc. Therefore, the accuracy of radiometric and geometric correction results has a significant impact on the detection accuracy. Moreover, in these methods, physical meaning of continuous spectral signatures is ignored.

Some transformation-based methods, e.g., conventional principal component analysis (CPCA) and temporal principal component analysis (TPCA) [6], multivariate alteration detection [7], and independent component analysis [8], project the hyperspectral data into another feature space to mark the changed pixels or areas. As an extension of change vector analysis (CVA) [9], compressed change vector analysis (C^2VA) [10] was proposed, which projects multiband information into 2-D polar representation, and distinguishes changed objects by a distance metric. These methods make full use of spectral information, but ignore adjacent pixels. To break this constraint, Liu *et al.* proposed a multiscale morphological compressed change vector analysis (M^2C^2VA) [11], where spatial information is included by using morphological processing. Subsequently, considering that unchanged pixels should be spectrally invariant and varying slowly, Wu *et al.* proposed a slow feature analysis (SFA) [12] method to transform the dataset into a new feature space. However, in the process of transformation, the structure of spectrum is inevitably destroyed.

The classification-based methods [13]–[15] are mainly divided into two categories, that is, postclassification method and direct classification method. The postclassification method is a relatively intuitive change detection algorithm, in which images of different time series are classified separately, and then, classification results are compared and analyzed. Since these images of different time series are classified separately, the influence of atmosphere, sensors, seasons, and other environmental factors on image acquisition can be eliminated. The direct classification method is to stack multitemporal images together, and uses a classifier to find changed categories. Because these methods adopt classification as the basis, a high-precision geometric registration between images is essential.

With the development of deep learning, deep learning-based methods [4], [16] have also become a research hotspot topic. Lyu *et al.* [17] proposed an end-to-end recurrent neural network (RNN) to solve the multispectral image change detection, where the RNN is a natural candidate to tackle the multitemporal dataset in change detection tasks. Subsequently, to generate rich spectral-spatial feature representations and effectively analyzes temporal dependence in bitemporal images, a recurrent 3-D fully convolutional neural network (ReCNN) [18] is used to process hyperspectral change detection task. However, there methods aim at generating a data-driven linear or nonlinear transformation to obtain robust features for change detection. Although they have achieved superior change detection results, they are often overfit and only effective for specific detection scenarios. These models, which are driven by data, rely on training datasets excessively, that is, the scale of training database data and the accuracy of labels determine the stability of these models. Therefore, these techniques are still under developing.

In addition, some other methods, which mainly include unmixing-based [3], [19], [20], low rank, sparse representation-based [21], etc., have also achieved a good detection accuracy in hyperspectral change detection. These hyperspectral change detection methods are developed according to different purposes. Although these hyperspectral change detection algorithms have been widely used, there are still some problems, including lacking of theoretical foundation and appropriate evaluation standards, high sensitivity of data preprocessing, poor versatility of the detection method, lacking of multisource data integration analysis, low utilization of spatial information during detection, etc. Therefore, how to increase the separability between changed pixels and background and accurately identify changed types, has become an important challenge in the current change detection task.

Traditional change detection methods treat hyperspectral image as a 2-D matrix by reshaping the original image along the spectral dimension. However, the actual hyperspectral image is a 3-D cube and the flattening operation of the matrix loses inherently spatial structure information. Therefore, in the processing of hyperspectral images, it is crucial to adopt a more effective representation method to cater for the structural characteristics of hyperspectral data. Recently, tensor-based method has shown potential to effectively represent the structural characteristics of high-dimensional data, and has achieved remarkable results in medical hyperspectral image classification [22], [23], infrared small target detection [24], [25], anomaly detection [26], [27], dimension reduction [28], [29], etc. Based on the tensor model and multilinear algebra, it has been demonstrated that tensor representation can simultaneously deal with the two spatial dimensions and one spectral dimension of hyperspectral data to achieve a satisfying performance.

However, to the best of our knowledge, there are few existing works on hyperspectral change detection using tensor representation. Zhao *et al.* introduced tensor into hyperspectral change detection by using 4-D higher order singular value decomposition (4D-HOSVD) [30], where bitemporal hyperspectral images were stacked together as a 4-D dataset for processing, in which change features were extracted by Tucker decomposition. Subsequently, Huang *et al.* combined tensor with deep learning to detect changed pixels or areas [31], where a tensor-based information model of underlying features change in hyperspectral images was established. However, these methods stack multitemporal images together for processing, which ignore the influence caused by various acquisition conditions. The motivation of this research is to retain the intrinsic spectral structure information for change detection from hyperspectral imagery. Different from [30], in this work, an effective hyperspectral change detection framework based on tensor decomposition and reconstruction is designed, where Tucker decomposition and high-order principal component (PC) extraction are adopted to process bitemporal images. In the reconstruction processing, the number of PCs is determined by the singular value energy accumulation method in different factor matrices. By the tensor theory, hyperspectral images can be represented as a third-order tensor, which well exploit the 3-D spatial and spectral information of multitemporal datasets.

The main contributions are summarized as follows.

1) Three-order Tucker decomposition is used to process subsequent hyperspectral images analysis, where Tucker decomposition and image reconstruction strategies are adopted to obtain more robust multitemporal hyperspectral datasets, and a singular value energy accumulation method is designed to determine the number of PCs in different factor matrices.
2) A new detector is developed to amplify the difference of heterogeneous pixels by making full use of the local spatial-spectral information of testing pixel, thereby improving the detection accuracy.
3) In different data domains (original data and reconstructed data), the difference between changed pixel pairs and unchanged pixel pairs is calculated, where spectral angle is used as metric to measure the degree of spectral difference. It is verified that Tucker decomposition can suppress difference of unchanged pixel pairs and effectively amplify difference of changed pixel pairs simultaneously.

The remainder of this article is organized as follows. In Section II, a detailed description of the proposed framework is presented. In Section III, five real datasets are utilized to verify the proposed method, and the experiment results and parameters are analyzed and discussed. Finally, Section IV concludes this article.

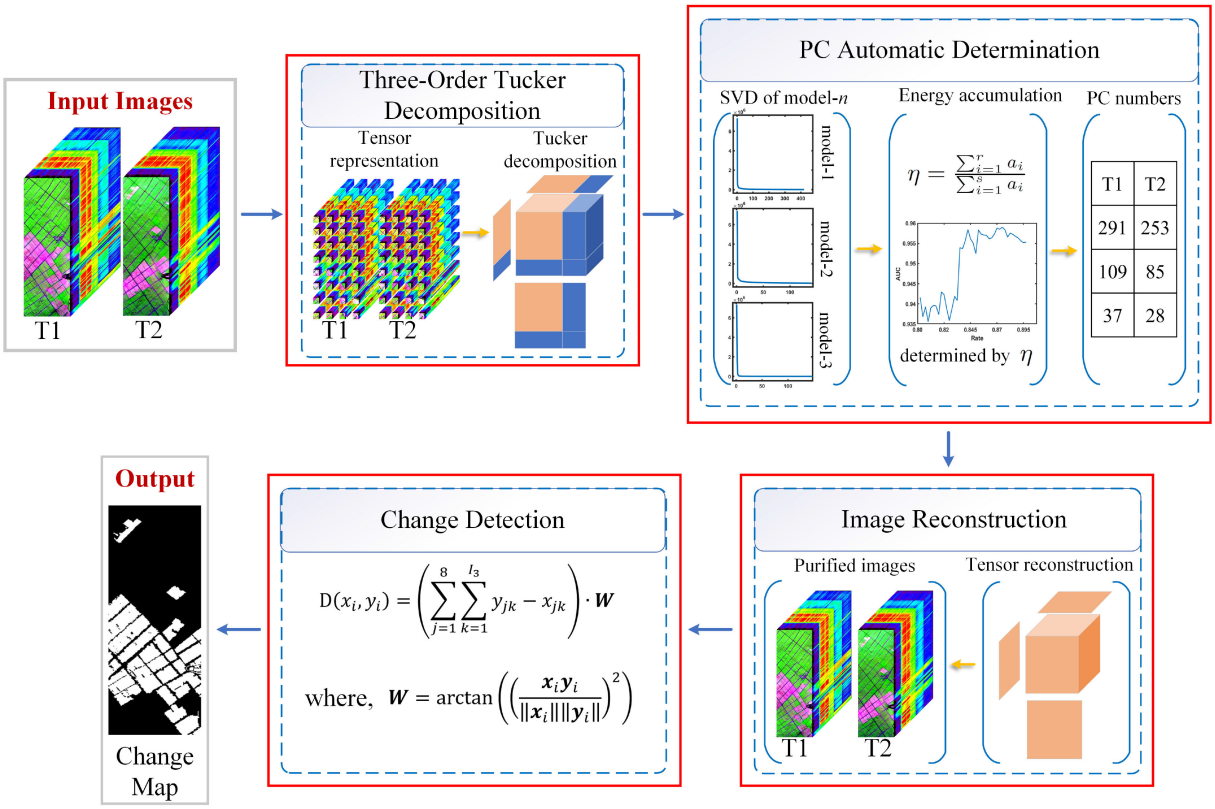

Fig. 1. Framework of proposed three-order Tucker decomposition-based hyperspectral change detection framework.

II. Proposed Change Detection Framework

Fig. 1 illustrates the flowchart of the proposed tensor-based hyperspectral change detection framework, called tensor decomposition and reconstruction detector (TDRD), which consists of the following steps. First, tensor representation is adopted to exploit structure information. Then, in order to eliminate the influence of changed factors, Tucker decomposition that can well exploit the 3-D spectral and spatial information of hyperspectral data is used to extract high-order PC information from multitemporal dataset. Finally, a especially designed detector is adopted to further improve the detection accuracy.

A. Three-Order Tensor Representation and Tucker Decomposition

The spectral variation of unchanged pixels caused by various factors is one of the main challenges of hyperspectral change detection. Therefore, solely using spectral information cannot effectively judge changed pixels or region. Taking into account the similarity of unchanged pixels in bitemporal images, tensor representation is adopted to incorporate 3-D spatial structure information of spectrum. Hyperspectral image can be represented as a three-order tensor $\boldsymbol{X} \in R^{I_1 \times I_2 \times I_3}$, where I_1, I_2, and I_3 represent the image rows, columns, and bands, which correspond to the mode-1, model-2, and mode-3, respectively.

Due to the influence of various factors (seasons, terrain, weather conditions, solar altitude angle, etc.), spectral curves of unchanged pixels in multitemporal have some differences. In order to obtain more robust feature, Tucker decomposition [26], [32] is employed to reconstruct multitemporal datasets. The tensor $\mathcal{X}$ can be approximately denoted by

$$\boldsymbol{X} \approx \mathcal{G} \times_1 \boldsymbol{U} \times_2 \boldsymbol{V} \times_3 \boldsymbol{W} \tag{1}$$

where $\mathcal{G} \in R^{I_1 \times I_2 \times I_3}$ is called the core tensor and its elements denote the level of interaction between distinct components. $\boldsymbol{U} \in R^{I_1 \times I_1}$, $\boldsymbol{V} \in R^{I_2 \times I_2}$, and $\boldsymbol{W} \in R^{I_3 \times I_3}$ are three factor matrices, which can be regarded as the PCs in each mode. The optimization problem is stated as

$$\begin{aligned} &\underset{\mathcal{G},\boldsymbol{U},\boldsymbol{V},\boldsymbol{W}}{\operatorname{argmin}} \ \|\mathcal{X} - \mathcal{G} \times_1 \boldsymbol{U} \times_2 \boldsymbol{V} \times_3 \boldsymbol{W}\|_2^F \\ &\text{s.t.} \begin{cases} \mathcal{G} \in R^{I_1 \times I_2 \times I_3} \\ \boldsymbol{U} \in R^{I_1 \times I_1}, \boldsymbol{V} \in R^{I_2 \times I_2}, \boldsymbol{W} \in R^{I_3 \times I_3} \\ \boldsymbol{U}^T\boldsymbol{U} = \boldsymbol{I_1}, \boldsymbol{V}^T\boldsymbol{V} = \boldsymbol{I_2}, \boldsymbol{W}^T\boldsymbol{W} = \boldsymbol{I_3}. \end{cases} \end{aligned} \tag{2}$$

Since $\boldsymbol{U}$, $\boldsymbol{V}$, and $\boldsymbol{W}$ are orthogonal to each other, and $\mathcal{G}$ is obtained by

$$\mathcal{G} \approx \mathcal{X} \times_1 \boldsymbol{U} \times_2 \boldsymbol{V} \times_3 \boldsymbol{W}. \tag{3}$$

Therefore, the optimization problem in (2) is converted as

$$\begin{aligned} &\underset{\boldsymbol{U},\boldsymbol{V},\boldsymbol{W}}{\operatorname{argmax}} \ \|\mathcal{X} \times_1 \boldsymbol{U} \times_2 \boldsymbol{V} \times_3 \boldsymbol{W}\|_2^F \\ &\text{s.t.} \begin{cases} \mathcal{G} \in R^{I_1 \times I_2 \times I_3} \\ \boldsymbol{U} \in R^{I_1 \times I_1}, \boldsymbol{V} \in R^{I_2 \times I_2}, \boldsymbol{W} \in R^{I_3 \times I_3} \\ \boldsymbol{U}^T\boldsymbol{U} = \boldsymbol{I_1}, \boldsymbol{V}^T\boldsymbol{V} = \boldsymbol{I_2}, \boldsymbol{W}^T\boldsymbol{W} = \boldsymbol{I_3}. \end{cases} \end{aligned} \tag{4}$$

The aforementioned equation is usually solved by the alternating least-squares algorithm [32], [33], where each factor matrix is obtained by eigenvalue decomposition when the other two matrices are fixed.

B. High-Order PC Extraction and Image Reconstruction

Generally, Tucker decomposition can be regarded as high-order principal component analysis (PCA) [34], [35], which offers a straightforward approach of compression for preserving the most significant information, with insignificant information being truncated. By Tucker decomposition, a three-order tensor matrix is decomposed into three factor matrices ($\boldsymbol{U}, \boldsymbol{V}$, and $\boldsymbol{W}$) and a core tensor $\mathcal{G}$, where the column of each factor matrix is regarded as eigenvectors under mode-n ($n = 1, 2, 3$), ordered by decreasing magnitude of corresponding eigenvalues. The larger the eigenvalue is, the more information it retains [26]. Therefore, significant information is obtained by truncating suitable r PCs. Therefore, how to find an optimal r becomes the key challenges to high-order PC extraction.

In this case, eigenvalues corresponding each factor matrices are different, so the ability of capturing significant information is also different. How to determine the number of r_i ($i =$ 1,2,3) for different factor matrices ($\boldsymbol{U}, \boldsymbol{V},$ and $\boldsymbol{W}$) is crucial. Unfortunately, there is no reliable way to automatically select an optimal value for r_i, so far. Therefore, the energy-cumulative method that computes the sum of eigenvalues one by one until the cumulative energy achieves a specified ratio η to all energy, is adopted to obtain the optimal parameter.

In this article, this method is also employed to determine the numbers of PCs in three factor matrices, described as follows. The singular values of three factors matrices are obtained by singular value decomposition operation. All the nonzero singular values are quite different and vary across several orders of magnitude, which indicates that singular values have different contributions to the factor matrix. Based on this phenomenon, several singular values that contribute the most to the factor matrix are selected. The number of selected singular values is taken as the number of PC corresponding to the factor matrix.

In bitemporal dataset, the change of singular values is relatively consistent, so three PC numbers corresponding three unfold modes, respectively, are selected to reconstruct the image. However, if this operation is required for every factor matrix, it is undoubtedly complicated and time consuming. Therefore, a strategy of automatically determining PC numbers through the accumulation of singular values is used, where a rate η needs to be determined by

$$\eta = \frac{\sum_{i=1}^{r} a_i}{\sum_{i=1}^{s} a_i} \tag{5}$$

where $a_i = [a_1, a_2, \ldots, a_s]$ is the singular value of the factor matrix, s is the number of all nonzero singular values, and r is the selected PC numbers. Therefore, by setting the value of η, the corresponding r in different factor matrices is automatically determined. η is set empirically. Generally, more complex the background, smaller the rate is.

Different from PCA, Tucker decomposition [26], [35] can effectively retain the spectral dimension. Simultaneously, other impurity signal is eliminated, which is essential for multitemporal images. By employing this operation, Tucker decomposition provides simple compression to preserve r_i PC for different factor matrices, which makes the original unchanged spectral signal in different time-series images suppressed, while the changed spectral signal is amplified. The reconstructed $\tilde{\mathcal{X}}$ has the same spectral dimension as the $\mathcal{X}$, which is obtained by

$$\tilde{\mathcal{X}} \approx \mathcal{G}_r \times_1 \boldsymbol{U}_{r_1} \times_2 \boldsymbol{V}_{r_2} \times_3 \boldsymbol{W}_{r_3} \tag{6}$$

where $\mathcal{G}_r = \mathcal{G}(1 : r_1, 1 : r_2, 1 : r_3)$, $\boldsymbol{U}_r = \boldsymbol{U}_r(:, 1 : r_1)$, $\boldsymbol{V}_r = \boldsymbol{V}_r(:, 1 : r_2)$, and $\boldsymbol{W}_r = \boldsymbol{W}_r(:, 1 : r_3)$. r_i is the PC number of the different factor matrix, which is determined by the aforementioned energy-cumulative method.

The PC numbers is determined automatically by setting empirical parameters η, but this strategy will inevitably be accompanied by a slight loss of significant information. However, it ensures that there is only one input parameter, which also further improves the simplicity and applicability.

Completing the reconstruction operation, a reconstructed tensor $\tilde{\mathcal{X}} \in R^{I_1 \times I_2 \times I_3}$ is obtained. After the same processing of bitemporal datasets is completed, the newly reconstructed datasets $\tilde{\mathcal{X}}_{T_1}$ and $\tilde{\mathcal{X}}_{T_2}$ corresponding to the scene at time T_1 and T_2, respectively, are carried out to change detection.

C. Change Detection for Reconstruction Datasets

In the acquisition of multitemporal dataset, due to complex environmental factors, it makes the spectral signals of unchanged pixel pairs have certain differences, which is also one of the main challenges in hyperspectral change detection. After tensor processing, multitemporal dataset is reconstructed, and spectral variation in unchanged pixel pairs becomes smaller, which is more conducive to the fully mining of neighborhood information of testing pixel. However, this change is difficult to be reflected in traditional detectors, because various detection algorithms are developed for different applications, which may not be suitable for these datasets after tensor processing. Therefore, it is necessary to develop a new detector that amplifies spectral variation of changed pixel pairs and suppress unchanged pixel pairs simultaneously.

In change detection, the difference in the digital number value is most intuitive. As a simple detector, AD has achieved satisfactory results in change detection, which adopts the analysis of corresponding pixels one by one, but it is easily affected by radiometric correction and geometric correction. Therefore, considering local background pixels have a great influence on the testing pixel, especially eight neighboring pixels around the testing pixel, which are consistent in both spectral dimension and spatial dimension, a newly designed detector is proposed for change detection to further improve the detection accuracy and robustness, which is expressed as

$$D(\boldsymbol{x}_i, \boldsymbol{y}_i) = \left(\sum_{j=1}^{8} \sum_{k=1}^{I_3} |y_{jk} - x_{jk}| \right) \cdot W \tag{7}$$

where I_3 denotes the number of bands, $\boldsymbol{x}_i$ and $\boldsymbol{y}_i$ represent testing pixel corresponding to the scene at time T_1 and T_2, respectively, and x_{jk} and y_{jk} are pixel values corresponding a single band in eight neighboring pixels.

The spectral angle reflects the degree of the similarity between pixels. The smaller the spectral angle, the higher the similarity. After tensor processing, spectral variation in unchanged pixel pairs becomes smaller, and spectral variation in change pixel pairs is amplified. Therefore, a spectral angle is an effective measure to judge whether pixel pairs have changed or not. In the designed detector, based on the core principle of the spectral angle, a especially designed revised spectral angle weighted W is adopted, which is expressed as

$$W = \arctan\left(\left(\frac{\boldsymbol{x}_i \boldsymbol{y}_i}{\|\boldsymbol{x}_i\|\|\boldsymbol{y}_i\|}\right)^2\right). \tag{8}$$

In the revised spectral angle weighted W, both $\arctan(\cdot)$ and power operation are monotonically increasing function, which are used to further amplify the spectral differences.

D. Spectral Analysis in Different Domains

Structural characteristics of hyperspectral data are effectively represented by tensors. Spectral signatures of the same substance obtained in various time phases have similar structures characteristics, which is helpful to improve the performance of the detector. Therefore, the hyperspectral data after tensor processing are more robust. To verify that the spectral difference of unchanged pixel pairs is effectively suppressed, while the differences of changed pixel pairs are further amplified, after tensor manipulation of bitemporal hyperspectral datasets, the spectral angle is used as a metric to analyze these differences.

As illustrated in Fig. 2, a changed pixel pair and a unchanged pixel pair are randomly selected from Yancheng dataset as an example to illustrate the spectral change before and after Tucker decomposition and reconstruction processing, where O_1 and O_2 represent the point selected at T_1 time and T_2 time in the original dataset space, respectively. Similarly, C_1 and C_2 represent the point selected at T_1 time and T_2 time in the tensor dataset space, respectively.

As shown in Fig. 2(a), the two red curves (in the original domain) become two black curves (in the tensor domain) after tensor processing, and the spectral difference between bitemporal is further narrowed. Obviously difference between red curves and black curves can be observed when abscissa of spectral curves is in the range of 75–85, and the trend of two black curves is closer compared to two red curves, which reflects that tensor processing can effectively suppress unchanged pixel pair's spectral variation in time-series images. On the contrary, in Fig. 2(b), when abscissa of spectral curves is in the range of 69–75, compared with two red spectral curves, the interval between two black spectral curves is smaller, which further confirms that after tensor processing, spectral variation of the changed pixel pair is further amplified.

Table I lists spectral angle values of two pairs randomly selected in the two domain. The spectral angle becomes smaller when the unchanged pixel pair is projected to the tensor domain,

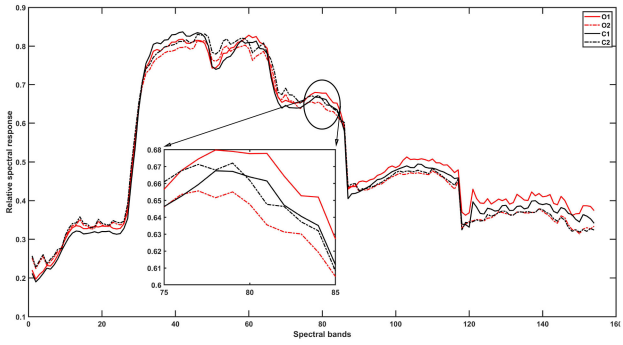

(a)

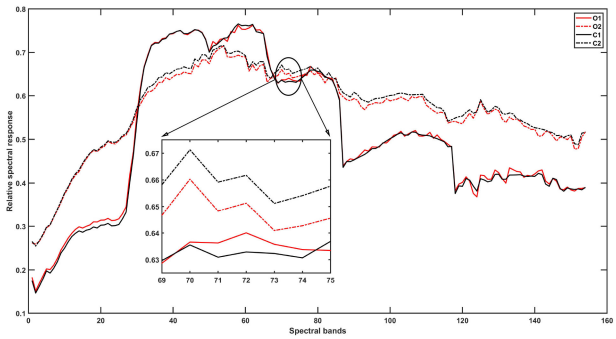

(b)

Fig. 2. Illustration of spectral change in Yancheng dataset. (a) Unchanged point spectrum. (b) Changed point spectrum.

TABLE I
SPECTRAL ANGLE VALUES UNDER DIFFERENT DOMAIN (NORMALIZED)

Categories	Unchanged point	Changed point
Original images	0.02847	0.11085
Tensor reconstructed images	0.02729	0.11339

TABLE II
ACCURACY COMPARISON UNDER DIFFERENT SAN FRANCISCO SCENES (AUC VALUES %)

Datasets	PCA+AD	RPCA+AD	Tucker+AD	TDRD
San Francisco1	50.682	63.271	66.740	74.156
San Francisco2	51.807	72.770	73.955	82.523

while the spectral angle of the changed pixel pair becomes larger. It further verifies that tensor processing can remarkably improve the separability of the changed and unchanged pixels.

E. Comparison With 2-D Low-Rank Recovery

In order to show the advantage over the 2-D low-rank recovery, the two pairs of San Francisco datasets (will be introduced in next *Section III-B*) containing speckle noise are used to analyze the performance of the 3-D Tucker decomposition and 2-D low-rank decomposition [i.e., robust PCA (RPCA)]. Table II lists change detection results of San Francisco scenes after Tucker decomposition and low-rank decomposition, where PCA [36], [37] and RPCA [38], [39] are employed to obtain low-rank parts. In PCA, the first three PCs that contain almost all the useful

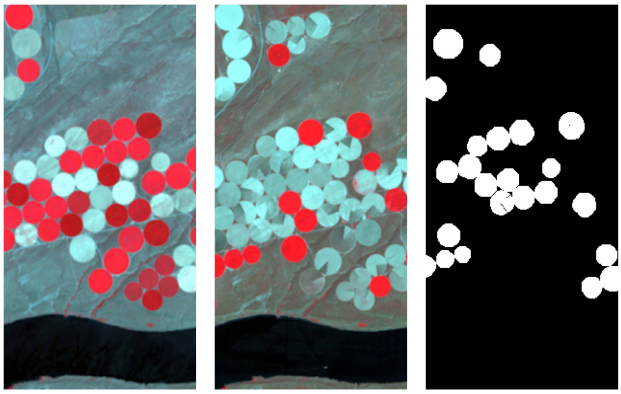

(a) (b) (c)

Fig. 3. Illustration of the Hermiston dataset. (a) Farmland on May 1, 2004. (b) Farmland on May 8, 2007. (c) Ground-truth change map.

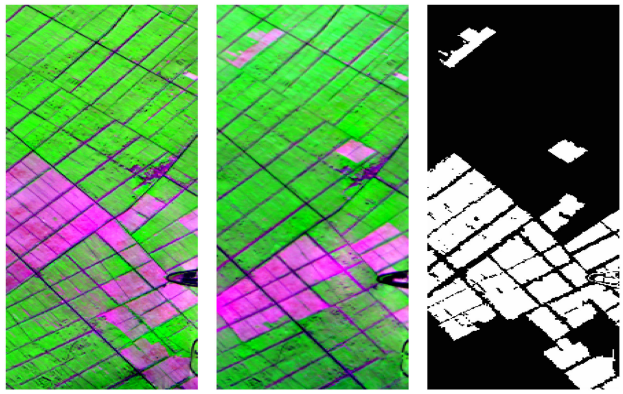

(a) (b) (c)

Fig. 4. Illustration of the Yancheng dataset. (a) Farmland on May 3, 2006. (b) Farmland on April 23, 2007. (c) Ground-truth change map.

information are retained. In RPCA, the data are decomposed into low-rank and sparse parts and the former one is used for change detection via AD. As listed in Table II, the dataset obtained by the 3-D low-rank decomposition has a better discrimination ability for changed objects compared with the dataset obtained by the 2-D decomposition. Furthermore, area under curve (AUC) values of Tucker+AD is greater than PCA+AD and RPCA+AD, while AUC values of the TDRD are greater than Tucker+AD, which further confirms that three-order Tucker decomposition has a greater contribution in a TDRD.

III. Experimental Results and Discussion

To evaluate performance of the proposed method, five bitemporal datasets are conducted to perform hyperspectral change detection. It is worth noting that these datasets, which are widely used in the field of hyperspectral changes, are obtained after preprocessing including atmospheric correction, geometric, and radiometric correction [18].

A. Hyperspectral Datasets

The first hyperspectral dataset is made of a pair of real bitemporal hyperspectral images, collected from an irrigated agricultural field in Hermiston City in Umatilla County, OR, USA, which were acquired by the Hyperion sensor mounted onboard the Earth Observing-1 (EO-1) satellite May 1, 2004 and May 8, 2007, respectively [40], [41]. The Hermiston images have the size of 390×200 pixels, and 242 spectral bands ranging from 0.4–2.5 μm. These images have a spectral resolution of 10 nm and a spatial resolution of 30 m. The main change on these datasets is farmland land-cover change, including the transitions among crops, soil, water, and other land-cover types. The change occurred in the cropland is mainly due to vegetation water content affected by irrigation condition and the difference in crop growth situation [41]. The scene and the ground-truth map are shown in Fig. 3.

The second dataset including two hyperspectral bitemporal images was obtained by EO-1 Hyperion sensor, which were collected over a wetland agricultural area in Yancheng city, Jiangsu Province, China, on May 3, 2006 and April 23, 2007, respectively [18]. Subset images with 420×140 pixels and 154 spectral bands were used after removing noisy and water-absorption bands. The images and the ground-truth map are illustrated in Fig. 4.

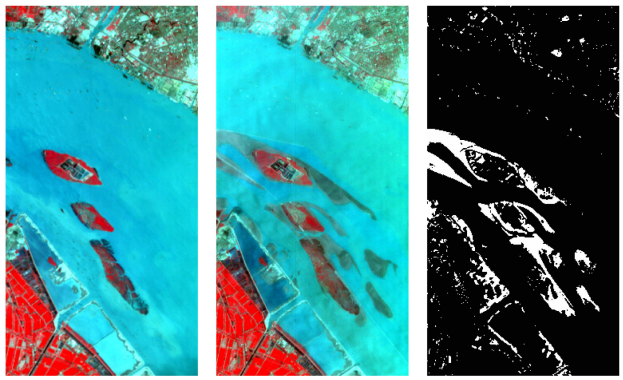

(a) (b) (c)

Fig. 5. Illustration of the River dataset. (a) River scene on May 3, 2013. (b) River scene on December 31, 2013. (c) Ground-truth change map.

The third dataset collected in Jiangsu Province, China, on May 3, 2013 and December 31, 2013, respectively, is the river scene, which contains two hyperspectral images for change detection. The sensor used is the EO-1 Hyperion, with a spectral range of 0.4–2.5 μm, a spectral resolution of 10 nm, a spatial resolution of 30 m, and a total of 242 spectral bands. The size of the image is 463×241 pixels, and 198 bands are used. The main change type is disappearance of the substance in the river [16], [40]. The images and the ground-truth map are illustrated in Fig. 5.

B. PolSAR Datasets

The fourth and fifth datasets are two pairs of single-look quad-polarimetric SAR images acquired by the UAVSAR airborne sensor in L-band over an urban area in San Francisco city on September 18, 2009, and May 11, 2015, respectively. These datasets are named San Francisco1 and San Francisco2,

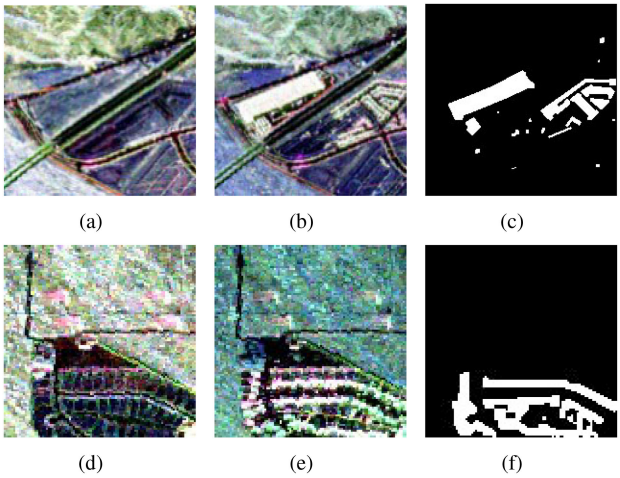

Fig. 6. Illustration of the San Francisco dataset. (a) Pauli image of San Francisco dataset1 on September 18, 2009. (b) Pauli image on May 11, 2015. (c) Ground-truth change map. (d) Pauli image of on September 18, 2009. (e) Pauli image on May 11, 2015. (f) Ground-truth change map.

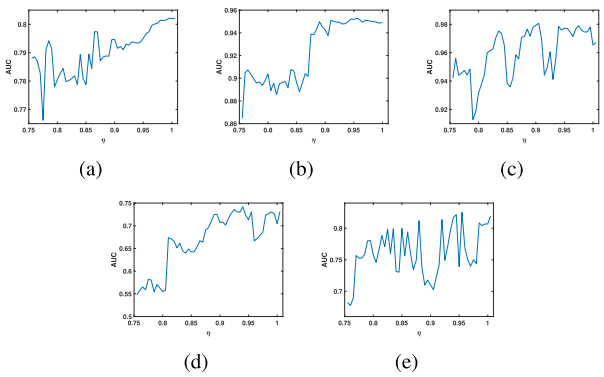

Fig. 7. AUC values under different η in various datasets. (a) Hermiston dataset. (b) Yancheng dataset. (c) River. (d) San Francisco1 dataset. (e) San Francisco2 dataset.

respectively. The size of San Francisco1 dataset is 200×200 pixels with 138 bands, and the size of San Francisco2 dataset is 100×100 pixels with 138 bands. The spatial resolution of two pairs PolSAR datasets are both 30 m. The detailed description can be found in [40] and [42].

C. Parameters Setting

In order to validate the proposed TDRD effectively, results derived by the proposed method are compared with those derived by eight other methods, including AD [5], absolute average difference (AAD) [43], [44], subspace-based change detection (SCD) [45], local SCD (LSCD) [45], adaptive SCD (ASCD) [45], ED [5], 4D-HOSVD [30], and M^2C^2VA [11].

For the proposed TDRD, the performance is relatively sensitive to the number of PCs. After a wealth of experimental analysis, it is found that the case of η not less than 0.75 is the basic condition to ensure the tensor operation in these datasets. Fig. 7 displays the influence of η on AUC values. When η changes, the detection result also changes, and the optimal η is different.

TABLE III
OPTIMAL PARAMETERS OF VARIOUS METHODS IN DIFFERENT DATASETS

Methods	LSCD(ω)	ASCD(ω)	TDRD(η)
Hermiston	3	13	0.990
Yancheng	3	3	0.955
River	3	3	0.900
San Francisco1	7	25	0.935
San Francisco2	7	21	0.950

A general conclusion is that when η reaches a certain value (between 0.9 and 1), the change of detection accuracy gradually becomes insignificant with further increase of η.

In these contrast methods such as LSCD and ASCD, their performance is sensitive to varying window sizes (ω). For window size, in LSCD and ASCD, by changing ω from 3 to 15, detection performance under different window sizes is collected, and then, the optimal parameter is selected [46]. The optimal parameters are listed in Table III. It is worth noting that in 4D-HOSVD and M^2C^2VA, after obtaining change features, the K-means algorithm is used to identify changed pixels, while the clustering center of K-means is random, yielding inferior performance in these datasets. Therefore, to better excavate the superiority of detectors, instead of K-means, AD is used to perform change detection.

D. Results and Discussion

Taking Yancheng dataset as an example, detection results of various algorithms are shown in Figs. 8 and 9. In Fig. 8, binary detection results are illustrated when the false alarm rate reaches 0.25, where the proposed TDRD achieves better detection result. It is further confirmed that compared with other detectors, the proposed TDRD has a stronger suppression ability to unchanged pixels and a better discrimination ability to changed pixels. Similarly, from the specific change detection rate (CDR) of various algorithms as listed in Table IV, the same conclusion can be drawn. When the false alarm rate reaches 0.25, the TDRD has better detection than others. In Fig. 9, 3-D detection results of various algorithms are more intuitive. In Fig. 9(d)–(f), it is clearly observed that SCD, LSCD, and ASCD suppresses unchanged and changed pixels simultaneously. Therefore, the height of the detected changed pixels in 3-D results is lower than that of other algorithms. Fig. 9(i) shows better detection than other algorithms, but still cannot offer obvious distinction.

To compare the performance of different methods, receiver operating characteristic (ROC) curve, AUC [47], and statistical separability analysis, also known as boxplot [48], are utilized for performance assessment. The statistical separability analysis is used to reflect the distribution characteristics and compare distribution characteristics of multiple groups of data. Essentially, the separability analysis is a statistical distribution map of detection results corresponding to changed and unchanged pixels. In statistical separability analysis, the upper and lower boundaries of boxes are 75% and 25% of statistical interval, respectively, while the 0%–25% and 75%–100% intervals are represented by dotted lines. Red box represents changed pixels and green box represents unchanged pixels, where the interval

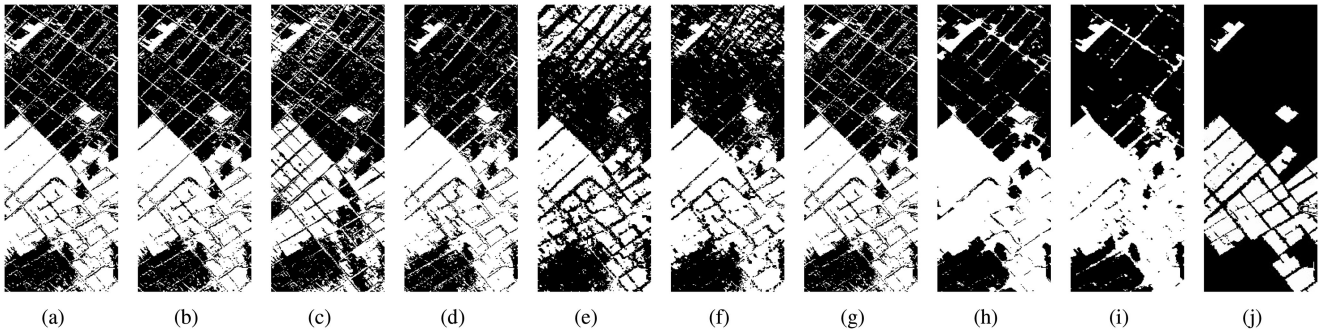

Fig. 8. Illustration of binary detection results when the false alarm rate reaches 0.25 in the Yancheng dataset. CDR: (a) AD:0.945. (b) ED:0.948. (c) AAD:0.768. (d) SCD:0.954. (e) LSCD:0.860. (f) ASCD:0.943. (g) 4D-HOSVD:0.945. (h) M^2C^2VA:0.969. (i) TDRD:0.973. (j) Ground truth.

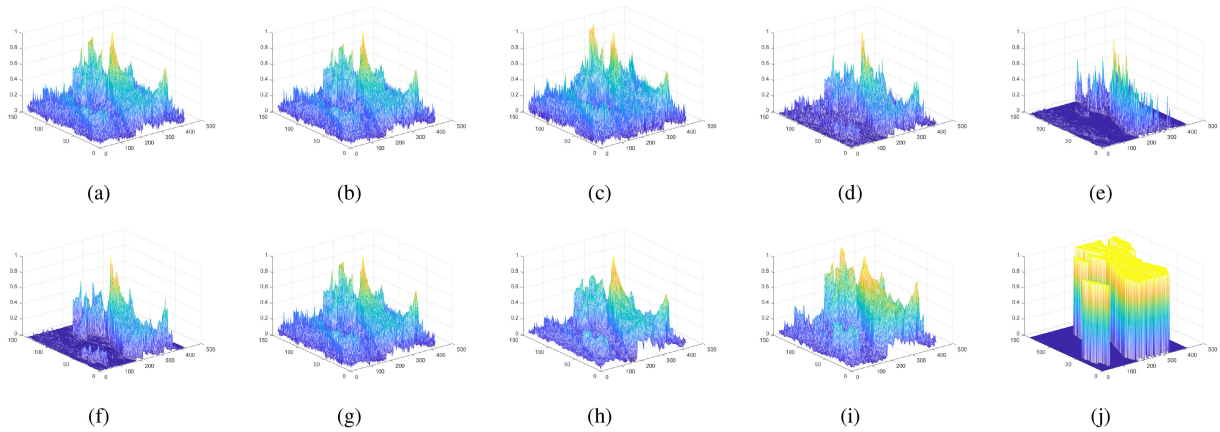

Fig. 9. Illustration of 3-D detection results in the Yancheng dataset. (a) AD. (b) ED. (c) AAD. (d) SCD. (e) LSCD. (f) ASCD. (g) 4D-HOSVD. (h) M^2C^2VA. (i) TDRD. (j) Ground truth.

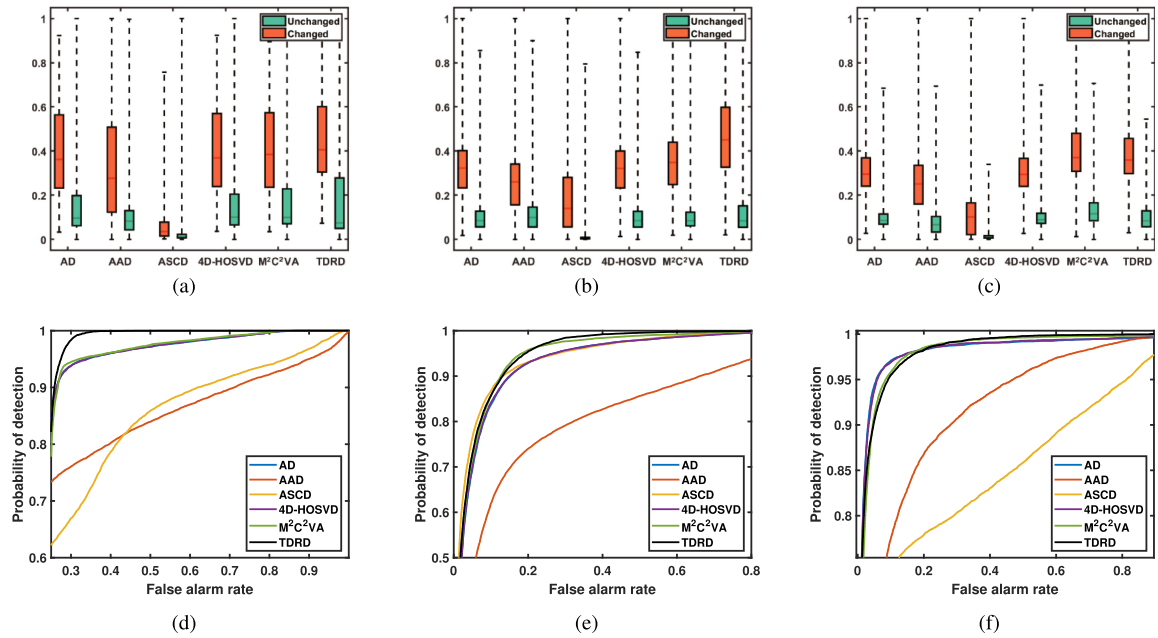

Fig. 10. Illustration of detection results. (a) Statistical separability analysis of Hermiston dataset. (b) Statistical separability analysis of Yancheng dataset. (c) Statistical separability analysis of River dataset. (d) ROC curves of Hermiston dataset. (e) ROC curves of Yancheng dataset. (f) ROC curves of River dataset.

TABLE IV
CHANGED DETECTION RATE ON YANCHENG DATASET WHEN FALSE ALARM RATE REACHES 0.25

Methods	AD [5]	ED [5]	AAD [44]	SCD [45]	LSCD [45]	ASCD [45]	4D-HOSVD [30]	M^2C^2VA [11]	TDRD
CDR	0.945	0.948	0.768	0.954	0.860	0.943	0.945	0.969	0.973

between red box and green box represents the separability. The height of the green box represents the suppression degree of these methods to unchanged pixels. Generally, the lower the green box height is, the stronger the unchanged pixel suppression is, which also translates into a better separation between changed and unchanged pixels.

As shown in Fig. 10(a)–(c), red and green boxes represent range of changed and unchanged pixels, respectively. The interval between red and green boxes represents the separability between changed and unchanged pixels. The height of the box represents suppression degree. Generally, lower the green box height is, stronger the unchanged pixel suppression is, which is also conducive to separating changed pixels from unchanged ones. In Fig. 10(a), the separability of Hermiston dataset is displayed, where the interval between red and green boxes of AD, 4D-HOSVD, and TDRD are obviously larger than other methods, which shows that these methods can separate changed pixels from unchanged pixels more effectively. Although the height of green boxes is lower in AAD and ASCD, which indicates that these methods can suppress unchanged pixels well, the interval between red and green boxes is smaller, which means that these methods cannot separate changed pixels. Similarly, for the Yancheng dataset shown in Fig. 10(b), the interval between red and green boxes of the proposed TDRD is obviously larger than other methods, which indicates that the TDRD can achieve change detection more effectively. In the ASCD, the height of the green box is significantly lower than others, which means that it has unchanged pixels better suppressed compared with other methods. However, its performance is poor, because it has poor ability of suppression and separation of changed pixels. In Fig. 10(c), the separability of River dataset is displayed, where the ASCD can suppress unchanged pixels well, but cannot separate changed pixels from unchanged pixels, while AD, 4D-HOSVD, M^2C^2VA, and TDRD can separate changed pixels from unchanged pixels more effectively.

In Hermiston dataset, ROC curves of different detection methods are illustrated in Fig. 10(d). It is easy to find that when the false alarm rate reaches about 0.25, the black ROC curve representing TDRD is obviously on the upper left corner, which reflects that the performance of the TDRD is better than other methods. In Yancheng dataset, as shown in Fig. 10(e), compared with other detection methods, the curve of the TDRD is obvious on the upper left corner, which confirms its effectiveness. In the River dataset, as shown Fig. 10(f), the same conclusion is obtained. The black curve representing the TDRD is slightly closer to the upper left corner than M^2C^2VA when the false alarm rate reaches about 0.2, which indicates that the TDRD has better detection performance than M^2C^2VA and other methods. Similarly, for the two pairs of SAR datasets as shown in Figs. 11 and 12, separability analysis and ROC curves are displayed. In Figs. 11(a) and 12(a), both changed and unchanged pixels

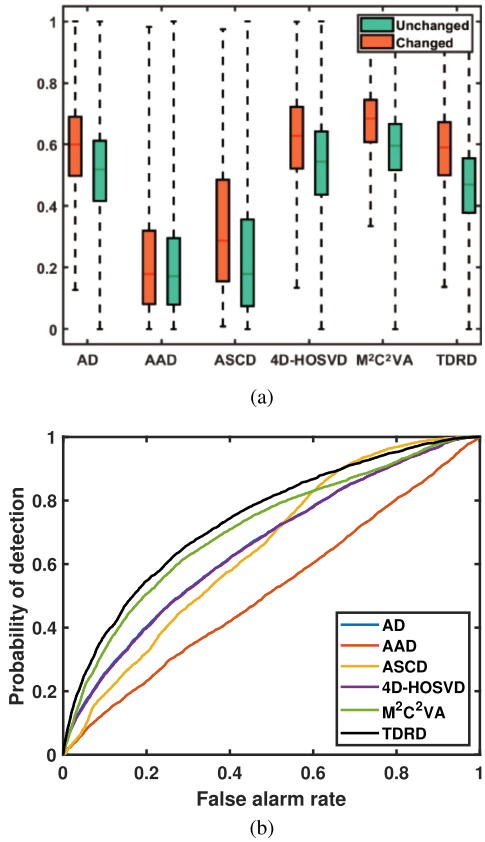

Fig. 11. ROC curves of different methods in the San Francisco1 dataset. (a) Statistical separability analysis. (b) ROC curves.

are severely suppressed in the ASCD, while changed pixels are well separated in the TDRD, compared with other detectors. Similarly, as shown in Figs. 11(b) and 12(b), the conclusion is that the TDRD has better detection performance than other methods.

Tables V and VI provide AUC values and computational cost of various detection methods, respectively. The detection results of the proposed TDRD are better than other methods for these datasets. By analyzing, it is further confirmed that the proposed TDRD is more effective than other traditional change detection methods, which shows that tensor can effectively improve the change detection ability. All the experiments are conducted on windows 10 with a 64-bit operating system. The processor of the system is Intel Core i7-8700 CPU with 3.20 GHz with 16 GB of main memory. As shown in Table VI, compared with other methods, the computational cost of the TDRD is high, especially for Hermiston dataset. The reason is that Tucker decomposition is time consuming.

TABLE V
ACCURACY COMPARISON OF BINARY CD ON DIFFERENT DATASETS (AUC VALUES %)

Methods	AD [5]	ED [5]	AAD [44]	SCD [45]	LSCD [45]	ASCD [45]	4D-HOSVD [30]	M^2C^2VA [11]	TDRD
Hermiston	78.582	79.662	77.828	68.348	68.236	74.111	78.595	78.369	**80.215**
Yancheng	93.696	93.667	81.365	93.443	89.878	94.545	93.751	94.927	**95.275**
River	98.002	97.944	91.582	95.038	74.182	85.530	98.043	97.927	**98.071**
San Francisco1	65.699	53.188	51.501	48.522	73.723	64.746	65.510	70.951	**74.156**
San Francisco2	73.134	60.547	49.238	60.466	79.234	71.270	72.821	74.982	**82.523**

TABLE VI
EXECUTION TIME OF VARIOUS METHODS USING DIFFERENT EXPERIMENTAL DATASETS (UNIT: SECONDS)

Methods	AD [5]	ED [5]	AAD [44]	SCD [45]	LSCD [45]	ASCD [45]	4D-HOSVD [30]	M^2C^2VA [11]	TDRD
Hermiston	0.040	0.069	0.043	0.215	20.495	28.042	2.752	15.451	14.756
Yancheng	0.020	0.040	0.024	0.150	12.418	1.608	1.553	9.145	7.014
River	0.048	0.082	0.050	0.295	27.165	3.353	3.732	14.411	17.347
San Francisco1	0.014	0.022	0.013	0.080	26.103	36.874	1.068	7.499	4.110
San Francisco2	0.003	0.006	0.003	0.019	6.350	6.587	0.275	5.909	1.132

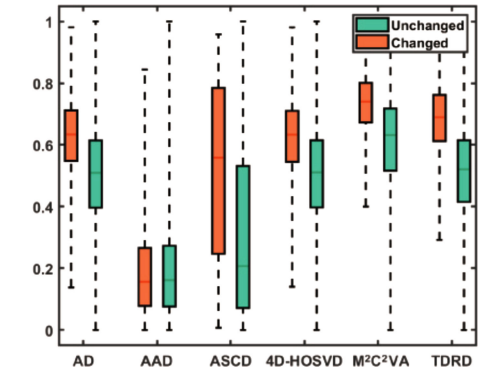

(a)

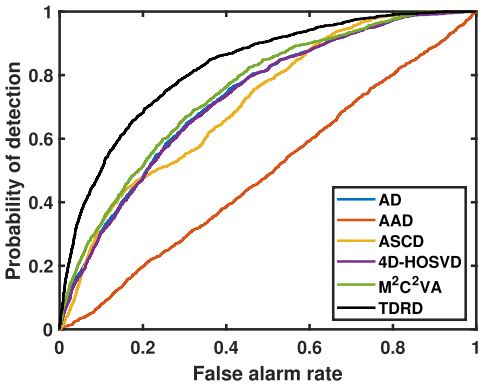

(b)

Fig. 12. ROC curves of different methods in the San Francisco2 dataset. (a) Statistical separability analysis. (b) ROC curves.

IV. CONCLUSION

In this article, a novel three-order Tucker decomposition and reconstruction-based change detection framework was designed, where Tucker decomposition and image reconstruction strategies were used to remove impurity signals in hyperspectral change detection. In the image reconstruction processing, PC numbers of various factor matrixes are determined by the singular value energy accumulation strategy. Meanwhile, a new detector was especially designed to detect changed pixels. Besides, spectral differences of unchanged pixel pairs and changed pixel pairs in different domains were analyzed. Low-rank decomposition and Tucker decomposition were also discussed, which further verify that tensor processing can better suppress unchanged pixel pairs, meanwhile amplify the difference of changed pixel pairs. The experiments results confirmed that the proposed method outperformed the traditional change detection methods. However, the computational cost of the proposed method is high, which will be the focus of our future work.

REFERENCES

[1] L. Bruzzone and F. Bovolo, "A novel framework for the design of change-detection systems for very-high-resolution remote sensing images," *Proc. IEEE*, vol. 101, no. 3, pp. 609–630, Mar. 2013.

[2] D. Marinelli, F. Bovolo, and L. Bruzzone, "A novel change detection method for multitemporal hyperspectral images based on binary hyperspectral change vectors," *IEEE Trans. Geosci. Remote Sens.*, vol. 57, no. 7, pp. 4913–4928, Jul. 2019.

[3] D. Hong, N. Yokoya, J. Chanussot, and X. X. Zhu, "An augmented linear mixing model to address spectral variability for hyperspectral unmixing," *IEEE Trans. Image Process.*, vol. 28, no. 4, pp. 1923–1938, Apr. 2019.

[4] B. Du, L. Ru, C. Wu, and L. Zhang, "Unsupervised deep slow feature analysis for change detection in multi-temporal remote sensing images," *IEEE Trans. Geosci. Remote Sens.*, vol. 57, no. 12, pp. 9976–9992, Dec. 2019.

[5] P. Du, S. Liu, P. Gamba, K. Tan, and J. Xia, "Fusion of difference images for change detection over urban areas," *IEEE J. Sel. Topics Appl. Earth Observ. Remote Sens.*, vol. 5, no. 4, pp. 1076–1086, Aug. 2012.

[6] V. Ortiz-Rivera, M. Vélez-Reyes, and B. Roysam, "Change detection in hyperspectral imagery using temporal principal components," *Proc. SPIE*, vol. 6299, 2006, Art. no. 623312.

[7] A. A. Nielsen, K. Conradsen, and J. J. Simpson, "Multivariate alteration detection (MAD) and MAF postprocessing in multispectral, bitemporal image data: New approaches to change detection studies," *Remote Sens. Environ.*, vol. 64, no. 1, pp. 1–19, 1998.

[8] S. Marchesi and L. Bruzzone, "ICA and Kernel ICA for change detection in multispectral remote sensing images," in *Proc. IEEE Int. Geosci. Remote Sens. Symp.*, 2009, vol. 2, pp. II-980–II-983, doi: 10.1109/IGARSS.2009.5418265

[9] W. A. Malila, "Change vector analysis: An approach for detecting forest changes with landsat," in *Proc. LARS Symposia*, 1980, pp. 326–335.

[10] F. Bovolo, S. Marchesi, and L. Bruzzone, "A framework for automatic and unsupervised detection of multiple changes in multitemporal images," *IEEE Trans. Geosci. Remote Sens.*, vol. 50, no. 6, pp. 2196–2212, Jun. 2012.

[11] S. Liu, Q. Du, X. Tong, A. Samat, L. Bruzzone, and F. Bovolo, "Multiscale morphological compressed change vector analysis for unsupervised multiple change detection," *IEEE J. Sel. Topics Appl. Earth Observ. Remote Sens.*, vol. 10, no. 9, pp. 4124–4137, Sep. 2017.

[12] C. Wu, B. Du, and L. Zhang, "Slow feature analysis for change detection in multispectral imagery," *IEEE Trans. Geosci. Remote Sens.*, vol. 52, no. 5, pp. 2858–2874, May 2014.
[13] F. Bovolo, L. Bruzzone, and M. Marconcini, "A novel approach to unsupervised change detection based on a semisupervised SVM and a similarity measure," *IEEE Trans. Geosci. Remote Sens.*, vol. 46, no. 7, pp. 2070–2082, Jul. 2008.
[14] B. Demir, F. Bovolo, and L. Bruzzone, "Detection of land-cover transitions in multitemporal remote sensing images with active-learning-based compound classification," *IEEE Trans. Geosci. Remote Sens.*, vol. 50, no. 5, pp. 1930–1941, May 2012.
[15] O. Ahlqvist, "Extending post-classification change detection using semantic similarity metrics to overcome class heterogeneity: A study of 1992 and 2001 us national land cover database changes," *Remote Sens. Environ.*, vol. 112, no. 3, pp. 1226–1241, 2008.
[16] Q. Wang, Z. Yuan, Q. Du, and X. Li, "Getnet: A general end-to-end 2-D CNN framework for hyperspectral image change detection," *IEEE Trans. Geosci. Remote Sens.*, vol. 57, no. 1, pp. 3–13, Jan. 2019.
[17] H. Lyu, H. Lu, and L. Mou, "Learning a transferable change rule from a recurrent neural network for land cover change detection," *Remote Sens.*, vol. 8, no. 6, p. 506, 2016.
[18] A. Song, J. Choi, Y. Han, and Y. Kim, "Change detection in hyperspectral images using recurrent 3 D fully convolutional networks," *Remote Sens.*, vol. 10, no. 11, p. 1827, 2018.
[19] S. Liu, L. Bruzzone, F. Bovolo, and P. Du, "Unsupervised multitemporal spectral unmixing for detecting multiple changes in hyperspectral images," *IEEE Trans. Geosci. Remote Sens.*, vol. 54, no. 5, pp. 2733–2748, May 2016.
[20] A. Ertürk, M.-D. Iordache, and A. Plaza, "Sparse unmixing with dictionary pruning for hyperspectral change detection," *IEEE J. Sel. Topics Appl. Earth Observ. Remote Sens.*, vol. 10, no. 1, pp. 321–330, Jan. 2017.
[21] C. Wu, B. Du, and L. Zhang, "Hyperspectral anomalous change detection based on joint sparse representation," *ISPRS J. Photogrammetry Remote Sens.*, vol. 146, pp. 137–150, 2018.
[22] M. Lv, W. Li, T. Chen, J. Zhou, and R. Tao, "Discriminant tensor-based manifold embedding for medical hyperspectral imagery," *IEEE J. Biomed. Health Inform.*, to be published.
[23] S. Velasco-Forero and J. Angulo, "Classification of hyperspectral images by tensor modeling and additive morphological decomposition," *Pattern Recognit.*, vol. 46, no. 2, pp. 566–577, 2013.
[24] M. Zhao, W. Li, L. Li, P. Ma, Z. Cai, and R. Tao, "Three-order tensor creation and tucker decomposition for infrared small-target detection," *IEEE Trans. Geosci. Remote Sens.*, to be published.
[25] L. Zhang and Z. Peng, "Infrared small target detection based on partial sum of the tensor nuclear norm," *Remote Sens.*, vol. 11, no. 4, p. 382, 2019.
[26] X. Zhang, G. Wen, and W. Dai, "A tensor decomposition-based anomaly detection algorithm for hyperspectral image," *IEEE Trans. Geosci. Remote Sens.*, vol. 54, no. 10, pp. 5801–5820, Oct. 2016.
[27] L. Li, W. Li, Y. Qu, C. Zhao, R. Tao, and Q. Du, "Prior-based tensor approximation for anomaly detection in hyperspectral imagery," *IEEE Trans. Neural Netw. Learn. Syst.*, to be published.
[28] L. Pan, H.-C. Li, Y.-J. Deng, F. Zhang, X.-D. Chen, and Q. Du, "Hyperspectral dimensionality reduction by tensor sparse and low-rank graph-based discriminant analysis," *Remote Sens.*, vol. 9, no. 5, p. 452, 2017.
[29] Y.-J. Deng, H.-C. Li, K. Fu, Q. Du, and W. J. Emery, "Tensor low-rank discriminant embedding for hyperspectral image dimensionality reduction," *IEEE Trans. Geosci. Remote Sens.*, vol. 56, no. 12, pp. 7183–7194, Dec. 2018.
[30] Z. Chen, B. Wang, Y. Niu, W. Xia, J. Q. Zhang, and B. Hu, "Change detection for hyperspectral images based on tensor analysis," in *Proc. IEEE Int. Geosci. Remote Sens. Symp.*, 2015, pp. 1662–1665.
[31] F. Huang, Y. Yu, and T. Feng, "Hyperspectral remote sensing image change detection based on tensor and deep learning," *J. Vis. Commun. Image Representation*, vol. 58, pp. 233–244, 2019.
[32] T. G. Kolda and B. W. Bader, "Tensor decompositions and applications," *SIAM Rev.*, vol. 51, no. 3, pp. 455–500, 2009.
[33] P. M. Kroonenberg, *Three-Mode Principal Component Analysis: Theory and Applications*, vol. 2. Leiden, The Netherlands: DSWO Press, 1983.
[34] L. De Lathauwer, B. De Moor, and J. Vandewalle, "A multilinear singular value decomposition," *SIAM J. Matrix Anal. Appl.*, vol. 21, no. 4, pp. 1253–1278, 2000.
[35] Q. Zhang, H. Wang, R. J. Plemmons, and V. P. Pauca, "Tensor methods for hyperspectral data analysis: A space object material identification study," *J. Opt. Soc. Amer. A*, vol. 25, no. 12, pp. 3001–3012, 2008.
[36] J. Deng, K. Wang, Y. Deng, and G. Qi, "PCA-based land-use change detection and analysis using multitemporal and multisensor satellite data," *Int. J. Remote Sens.*, vol. 29, no. 16, pp. 4823–4838, 2008.
[37] S. Wold, K. Esbensen, and P. Geladi, "Principal component analysis," *Chemometrics Intell. Lab. Syst.*, vol. 2, no. 1–3, pp. 37–52, 1987.
[38] F. De la Torre and M. J. Black, "Robust principal component analysis for computer vision," in *Proc. 8th IEEE Int. Conf. Comput. Vis*, 2001, pp. 362–369.
[39] E. J. Candés, X. Li, Y. Ma, and J. Wright, "Robust principal component analysis?" *J. ACM*, vol. 58, no. 3, pp. 1–37, 2011.
[40] S. T. Seydi, M. Hasanlou, and M. Amani, "A new end-to-end multi-dimensional CNN framework for land cover/land use change detection in multi-source remote sensing datasets," *Remote Sens.*, Multidisciplinary Digital Publishing Institute, vol. 12, no. 12, p. 2010, 2020.
[41] L. Bruzzone, S. Liu, F. Bovolo, and P. Du, "Change detection in multitemporal hyperspectral images," in *Multitemporal Remote Sensing*. Cham, Switzerland: Springer, 2016, pp. 63–88.
[42] A. Najafi, M. Hasanlou, and V. Akbari, "Land cover changes detection in polarimetric SAR data using algebra, similarity and distance based methods," Int. Arch. Photogramm. Remote Sens. Spatial Inf. Sci., vol. 42, pp. 195–200, 2017.
[43] C. Kwan, "Methods and challenges using multispectral and hyperspectral images for practical change detection applications," *Information*, vol. 10, no. 11, p. 353, 2019.
[44] J. Zhou, C. Kwan, B. Ayhan, and M. T. Eismann, "A novel cluster kernel RX algorithm for anomaly and change detection using hyperspectral images," *IEEE Trans. Geosci. Remote Sens.*, vol. 54, no. 11, pp. 6497–6504, Nov. 2016.
[45] C. Wu, B. Du, and L. Zhang, "A subspace-based change detection method for hyperspectral images," *IEEE J. Sel. Topics Appl. Earth Observ. Remote Sens.*, vol. 6, no. 2, pp. 815–830, Apr. 2013.
[46] X. Kang, X. Zhang, S. Li, K. Li, J. Li, and J. A. Benediktsson, "Hyperspectral anomaly detection with attribute and edge-preserving filters," *IEEE Trans. Geosci. Remote Sens.*, vol. 55, no. 10, pp. 5600–5611, Oct. 2017.
[47] J. A. Hanley and B. J. McNeil, "The meaning and use of the area under a receiver operating characteristic (ROC) curve," *Radiology*, vol. 143, no. 1, pp. 29–36, 1982.
[48] K. Tan, Z. Hou, F. Wu, Q. Du, and Y. Chen, "Anomaly detection for hyperspectral imagery based on the regularized subspace method and collaborative representation," *Remote Sens.*, vol. 11, no. 11, p. 1318, 2019.

Zengfu Hou received the B.S. degree in surveying and mapping engineering from the Hebei University of Engineering, Handan, China, in 2015, and the M.S. degree in photogrammetry and remote sensing from the China University of Mining and Technology, Xuzhou, China, in 2019. He is currently working toward the Ph.D. degree in information and communication engineering from the School of Information and Electronics, Beijing Institute of Technology, Beijing, China. He is an Active Reviewer for the IEEE TRANSACTIONS ON GEOSCIENCE AND REMOTE SENSING, IEEE SIGNAL PROCESSING LETTERS, and IEEE JSTARS. His research interests include hyperspectral anomaly detection, hyperspectral target detection, hyperspectral change detection, and pattern recognition.

His research interests include hyperspectral anomaly detection, hyperspectral target detection, hyperspectral change detection, and pattern recognition.

Wei Li (Senior Member, IEEE) received the B.E. degree in telecommunications engineering from Xidian University, Xi'an, China, in 2007, the M.S. degree in information science and technology from Sun Yat-Sen University, Guangzhou, China, in 2009, and the Ph.D. degree in electrical and computer engineering from Mississippi State University, Starkville, MS, USA, in 2012.

He spent one year as a Postdoctoral Researcher with the University of California at Davis, Davis, CA, USA. He is currently a Professor and the Vice Dean with the College of Information Science and Technology, Beijing University of Chemical Technology, Beijing, China. His research interests include hyperspectral image analysis, pattern recognition, and data compression.

Dr. Li was the recipient of the 2015 Best Reviewer Award from the IEEE Geoscience and Remote Sensing Society for his service for the IEEE JOURNAL OF SELECTED TOPICS IN APPLIED EARTH OBSERVATIONS AND REMOTE SENSING (JSTARS). He is an Active Reviewer for the IEEE TRANSACTIONS ON GEOSCIENCE AND REMOTE SENSING, IEEE GEOSCIENCE REMOTE SENSING LETTERS, and IEEE JSTARS. He is currently an Associate Editor for the IEEE SIGNAL PROCESSING LETTERS. He has served as a Guest Editor for special issue of the *Journal of Real-Time Image Processing*, *Remote Sensin*g, and the IEEE JSTARS.

Ran Tao (Senior Member, IEEE) received the B.S. degree in Hefei College of Electronic Engineering, Hefei, China, in 1985 and the M.S. and Ph.D. degrees from Harbin Institute of Technology, Harbin, China, in 1990 and 1993, respectively. After completing postdoctoral studies in electronics and communications at the Beijing Institute of Technology (BIT), China, he became an Associate Professor in 1996 and a Professor in 1999. From March 2001 to April 2002, he was a visiting scholar in the University of Michigan, Ann Arbor. He is currently a Professor with School of Information and Electronics, Beijing Institute of Technology, Beijing, China.

Prof. Tao was the recipient of the National Science Foundation of China for Distinguished Young Scholars in 2006, and the First Prize of Science and Technology Progress in 2006 and 2007, and the First Prize of Natural Science in 2013, both awarded by the Ministry of Education. He was a Distinguished Professor of the Changjiang Scholars Program in 2009. He was a Chief Professor of the Program for Changjiang Scholars and Innovative Research Team in University from 2010 to 2012. He has been a Chief Professor with the Creative Research Groups, National Natural Science Foundation of China, since 2014. He is currently the Vice Chair of the IEEE China Council and the URSI China Council.

Qian Du (Fellow, IEEE) received the Ph.D. degree in electrical engineering from the University of Maryland, Baltimore, MD, USA, in 2000.

She is currently the Bobby Shackouls Professor with the Department of Electrical and Computer Engineering, Mississippi State University, Starkville, MS, USA. Her research interests include hyperspectral remote sensing image analysis and applications, pattern classification, data compression, and neural networks.

Dr. Du is a Fellow of the International Society for Optics and Photonics. She was the recipient of the 2010 Best Reviewer Award from the IEEE Geoscience and Remote Sensing Society. She was a Co-Chair of the Data Fusion Technical Committee of the IEEE Geoscience and Remote Sensing Society from 2009 to 2013, and the Chair of the Remote Sensing and Mapping Technical Committee of the International Association for Pattern Recognition from 2010 to 2014. She is the General Chair of the 4th IEEE GRSS Workshop on Hyperspectral Image and Signal Processing: Evolution in Remote Sensing, Shanghai, in 2012. She has served as an Associate Editor for the IEEE JOURNAL OF SELECTED TOPICS IN APPLIED EARTH OBSERVATIONS AND REMOTE SENSING, the *Journal of Applied Remote Sensing*, and the IEEE SIGNAL PROCESSING LETTERS. Since 2016, she has been the Editor-in-Chief for the IEEE JOURNAL OF SELECTED TOPICS IN APPLIED EARTH OBSERVATIONS AND REMOTE SENSING.